Converting waste poly(ethylene terephthalate) to hierarchical porous carbon towards high-performance supercapacitor

Kaile Wang,[a] Ruiyang Li, [a] Xuesen Zeng,[b] Pingan Song[c,]*, Jisheng Sun,[d] Rongjun Song [a],*

[a] *Heilongjiang Key Laboratory of Molecular Design and Preparation of Flame Retarded Materials, College of Chemical Engineering and Resource Utilization, Northeast Forestry University, Harbin 150040, PR China*

b Centre for Future Materials, University of Southern Queensland, Toowoomba 4305, Queensland, Australia

c Centre for Future Materials, School of Agriculture and Environmental Science, University of Southern Queensland, Springfield 4300, Queensland, Australia

d Australia Sunlight Group Pty Ltd, Carole Park 4300, Queensland, Australia

* Corresponding author:

E-mail: pingan.song@usq.edu.au, pingansong@gmail.com

E-mail: rongjunsong@nefu.edu.cn

Abstract:

The annual massive production of polyethylene terephthalate (PET) has generated a large amount of waste and thus raised a widespread environmental concern. Converting waste PET into porous carbon materials represents a promising sustainable and green method to reduce its burden on the environment. However, there have been some key challenges with existing carbonization methods, such as complicated carbonization process, and the extensive use of corrosive activators. To overcome this challenge, we here propose a mild and efficient one-step pyrolysis strategy that can convert waste PET to hierarchical porous carbon (HPC) using K_2CO_3 as an activator/template. The resulting HPC-700 shows a unique interconnected

hierarchical porous structure and a higher oxygen content at a carbonization temperature of 700°C. The as-prepared HPC-based supercapacitor exhibits an exceptionally high specific capacitance of 332.3 F g^{-1} at a current density of 0.5 A g^{-1}, far higher than those of previous PET-derived carbon counterparts, in addition to an excellent rate capability and a high cycling stability with 95.98% capacitance retention after 10,000 cycles. This work offers a facile and effective approach to converting waste PET to porous carbon materials, which shows great potential applications for high-performance capacitors and other energy storage materials. In addition, this study conducted a life cycle assessment (LCA) to understand the ecological impact of the material conversion process.

Keywords: PET; Waste plastics; Hierarchical porous carbon; Capacitors; Energy storage

1. Introduction

Plastics are used widely in all aspects of daily life since their synthesis because of their low cost and excellent performances.[1] Globally, about 400 million plastics are produced and their production is predicted to be quadruple by 2050.[2] Among these plastics, polyethylene terephthalate (PET) has been widely used as plastics, fibers and textiles and others. The mass production of PET products however generates a massive amount of waste, which causes serious environmental issues if the waste is not recycled properly.[3] Generally, the majority of waste PET is physically recycled to remake new products and items. In parallel, many attempts have been made to chemically decompose PET into useful fine chemicals. For example, Tournier, V. *et al.* modified leaf-branch compost cutinase (LCC) to prepare one of the most efficient PET hydrolases that can hydrolyzes PET into terephthalic acid (TPA), ethylene glycol (EG), and mono(2-hydroxyethyl) terephthalate (MHET).[4] Likewise, Cao *et al.* reported the use of a Fe/ZnO nanosheet catalyst rich in oxygen vacancies to decompose PET into dimethyl terephthalate (DMT) and bis-2-hydroxyethyl terephthalate (BHET) via alcoholysis.[5] However, these techniques often require complicated synthesis or entail the use of expensive chemical reagents, which thus significantly impedes their practical application for recycling waste PET.

In the meantime, new green renewable energy sources and energy storage devices have been intensively investigated because it provides one possible solution to reducing carbon emission and mitigating global warming in the last years.[6] As a type of emerging energy storage device, supercapacitors feature high power density (more than 10 times that of secondary batteries), wide temperature ranges, long cycle life, fast charging and discharging, and no pollution to the environment.[7] Generally, the performance of supercapacitors is significantly determined by the physical and chemical properties of their electrode materials. Carbon materials are regarded as the most promising electrode material of supercapacitors because of their high electrical conductivity, tunable pore structures, and excellent thermal stability. Carbon sources are widely available. Biomass is easily accessible and inexpensive, but its low carbon content affects the carbon yield. Compared to waste plastics, biomass typically has a more complex structure and often requires more intricate pretreatment processes, such as low-temperature pretreatment to remove functional groups and increase defects[8], high-temperature carbonization, or sulfuric acid carbonization[9]. Additionally, highly corrosive chemicals like KOH are often used as activators, thereby posing potential environmental risks. While the use of activators increases the specific surface area, it also results in a single pore structure, primarily consisting of micropores, which increases the resistance to electrolyte ion transport in porous carbon and reduces the yield. Moreover, biomass-derived porous carbon, due to its higher impurity content, often requires the addition of conductive agents, such as acetylene black, for their use in supercapacitors. In contrast, waste PET has a high carbon content, a simple composition, but most of existing recycling methods have caused significant environmental issues. Therefore, it is crucial to recycle waste PET via a more sustainable manner.

In this context, the conversion of waste PET into carbon materials for electrochemical energy storage applications represents another promising strategy for recycling waste PET. Indeed, the last years have witnessed some encouraging advances in this recycling direction.[8-10] A typical example is that Reddygunta *et al.* used KOH as an activator to turn waste PET into porous carbon for preparing flexible supercapacitors which achieved a specific capacitance

of 228.2 F g^{-1} at a current density of 1 A g^{-1} in 1 M Na_2SO_4 electrolyte.[10] Meanwhile, *Chen et al.* prepared a waste PET-derived three-dimensional (3D) meso-/macro-porous carbon using MgO as an catalyst and template, and the resultant capacitor gave rise to a specific capacitance of 191.4 F g^{-1} at the current density of 0.5 A g^{-1}.[11] Mu *et al.* reported the direct catalytic carbonization of waste PET using a hybrid catalyst, MgO/$Co(acac)_3$ in an autoclave, leading to 3D porous carbon nanosheets. The resulting carbon electrode exhibited a specific capacitance of 210.5 F g^{-1} and excellent cyclic stability after 5000 cycles at 10 A g^{-1}.[12] Despite these advances, most of these carbonization processes are relevantly complicated and involve the use of highly corrosive chemicals (e.g., KOH), inevitably leading to potential environmental issues.

Therefore, this work aims to develop a facile, efficient and sustainable carbonization approach for converting waste PET to high-quality porous carbon materials. Unlike the chemicals used previously, K_2CO_3 is proposed to use as a catalyst and pore template by physically mixing with waste PET followed by direct carbonization in an inert gas atmosphere. The resultant hierarchical porous carbon (HPC) materials are highly graphitized in the shape of thin layers. The pore structures of the HPC can be readily controlled by adjusting the pyrolysis temperature. The HPC-700 (carbonized at 700°C)-based capacitor exhibited an ultra-high specific capacitance of 332.27 F g^{-1} at a current density of 0.5 A g^{-1}, much higher than those of previous PET-derived carbon electrode materials. Moreover, it demonstrates a 80.30% capacitance retention at a high current density of 20 A g^{-1} and a capacitance retention of 95.98% after 10,000 cycles, indicating its excellent rate capability and stability. This work provides a facile promising carbonization method by converting waste PET into high-quality carbon materials, which show great potential for energy storage applications.

2. Experimental Section

2.1 Synthesis of hierarchical porous carbon (HPC)

Waste PET bottles were collected from daily life sources. **Fig. 2a** depicts the synthetic route of hierarchical porous carbon (HPC) from waste PET. After the removal of caps and labels, the waste PET bottles were cleaned twice with ethanol and deionized water to remove

adhesive residues, followed by cutting into small pieces. The waste PET/K_2CO_3 mixture (mass ratio = 1/4) was obtained by thoroughly mixing waste PET (2.50 g) with K_2CO_3. The mixture was then carbonized at varied temperatures, 600 °C, 700 °C and 800 °C for 2 h in an N_2 atmosphere, respectively. Then, the obtained product was dried after washing with 2 M HCl for 12 h and deionized water. The samples obtained were named HPC-x (x = 600,700,800, representing the carbonization temperature, respectively). In addition, to further demonstrate the applicability of this method to other waste plastics, we selected seven types of waste plastics to prepare porous carbon, including Polyamide (PA), Polycarbonate (PC), Polystyrene (PS), High-Density Polyethylene (HDPE), Polypropylene (PP), Polylactic Acid (PLA), and mixed plastic waste (MPW). The proportions of low-density polyethylene (LDPE), HDPE, PP, PET, and PS in the MPW sample were 27%, 20.1%, 30.57%, 12.9%, and 9.43%, respectively, based on the relative production proportions of these different plastics.[13] The ratio of each plastic to K_2CO_3 was set at 1:4, with a reaction temperature of 700°C, and the resulting porous carbons were named C-x.

2.2 Material characterization

The morphology and microstructure of HPC were characterized using scanning electron microscopy (SEM; JSM-7500F) and transmission electron microscopy (TEM; JEM-2010). The crystal structures were characterized using a powder X-ray diffractometer (XRD; TD3500). The degree of graphitization of HPC was characterized using a Raman spectrometer (DXR2) with a 532 nm laser as the excitation source. The bond types and chemical structure/compositions of the obtained HPC materials were analyzed by X-ray photoelectron spectroscopy (XPS; Thermo Scientific ESCALAB 250Xi). Nitrogen adsorption/desorption equations for the samples were obtained using a gas adsorption analyzer (BELSORP MAX) at the temperature of liquid nitrogen (77 K). The specific surface area was calculated using the Brunauer-Emmett-Teller (BET) method, and the pore distribution was calculated using the BJH and HK methods.

2.3 Electrochemical performance testing

The electrochemical properties of the samples were tested at room temperature using an electrochemical workstation (CHI 660E). The active electrode material was prepared by ultrasonically dispersing 37.5 mg of the HPC sample and 50 μL of polytetrafluoroethylene binder (50 g L^{-1}) in an appropriate amount of ethanol. The mixture was dried and then pressed onto a clean nickel foam collector with a coating area of 1 × 1 cm^2 and a thickness of 1 mm. Finally, the prepared working electrodes were dried overnight in an oven at 65 °C. The counter electrode consisted of a network of platinum sheets, and the reference electrode comprised a mercury/mercury oxide electrode.

The selected electrolyte was a 6 M potassium hydroxide (KOH) solution. The electrochemical properties of the HPCs were characterized through cyclic voltammetry (CV), galvanostatic charge-discharge (GCD), and electrochemical impedance spectroscopy (EIS). Meanwhile, this experiment used two identical working electrodes to form a symmetrical dual-electrode supercapacitor, and the electrolyte was 1M sodium sulfate (Na_2SO_4) solution. All activated samples were tested at least three times to ensure the reproducibility of the results. In the three-electrode configuration, the specific capacitance of the electrode was calculated using the GCD (Galvanostatic Constant Current Discharge) curve by the following equation:

$$C_{GCD} = \frac{I \times \Delta t}{m \times \Delta U} \quad (1)$$

Where C_{GCD} (F g^{-1}) is the specific capacitance calculated from the GCD test, m (g) is the mass of the graded porous carbon loaded on the working electrode, I (A g^{-1}) is the current density of the discharge, Δt (s) is the time of the discharge process, and ΔU (V) is the actual potential difference during the discharge process.

For symmetric supercapacitor, the following formulas were used to calculate the energy density (E, Wh kg^{-1}) and power density (P, W kg^{-1}):

$$C_{cell} = \frac{I \times \Delta t}{2 \times m \times \Delta U} \quad (2)$$

$$E = \frac{C_{cell} \times (\Delta U)^2}{2 \times 3.6} \quad (3)$$

$$P = \frac{E}{\Delta t} \times 3600 \quad (4)$$

C_{cell}(F g^{-1}) is the specific capacitance obtained from the GCD curve of the two-electrode system. m (g) represents the loading mass of single electrode. ΔU (V) refers to the actual voltage window during the discharge process. Δt (s) represents the discharge time.

2.4 Life cycle assessment (LCA)

LCA compiles and evaluates the inputs, outputs, and potential environmental impacts of a product system across its entire life cycle. The LCA in this study aims to evaluate the environmental impacts of producing porous carbon from waste PET bottles via one-step carbonization for use as a supercapacitor electrode material.[14] **Fig. 1** shows the system boundary based on the gate-to-gate method, including pretreatment, carbonization, as well as water washing and drying. The function unit for research activities of LCA in this study was defined as 1 kg HPC-700.

The life cycle assessment study was conducted using OpenLCA with the Ecoinvent 3.9.1 database. The LCA followed the EF3.1, CML 4.8 and ReCiPe 2016 methods and included 10 impact categories: cumulative Energy Demand (CED), global warming potential (GWP), abiotic depletion potential (ADP), resource depletion-water (WU), eutrophication (EP), , acidification (AP), particulate matter (RI), photochemical ozone formation (POFP), ionizing radiation-human health effects (IRP), and ecotoxicity-freshwater (ET). These categories are frequently applied in research on waste and energy treatment. In addition, the experimental data are derived from laboratory-scale experiments, energy consumption estimates based on this may be significantly higher. However, the mass conversion rate is less affected by the scale of the operation. Therefore, it is more reasonable to use industrial-scale PET pyrolysis data to estimate the energy consumption during the carbonization, washing, and drying processes. Moreover, diesel lorry transportation for 30 km will be considered for cycled PET bottles. The amount of electricity consumed during the experiment is shown in **Table S1**.

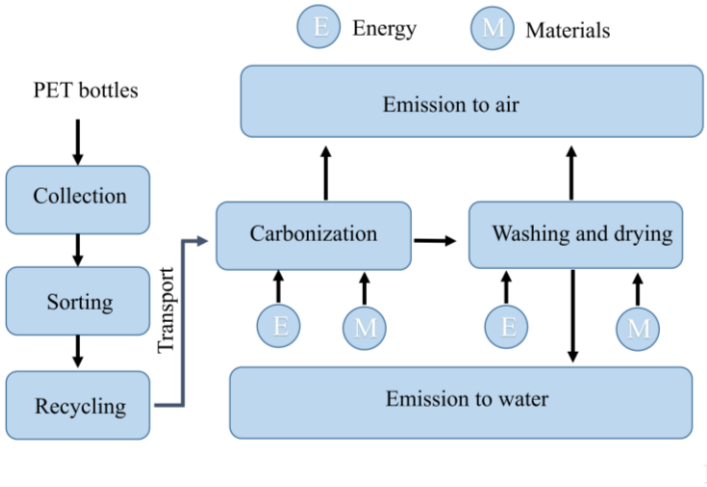

Fig. 1. System boundaries for LCA of porous carbon production from waste PET bottles.

3. Results and discussion

3.1. Characteristics of porous carbons

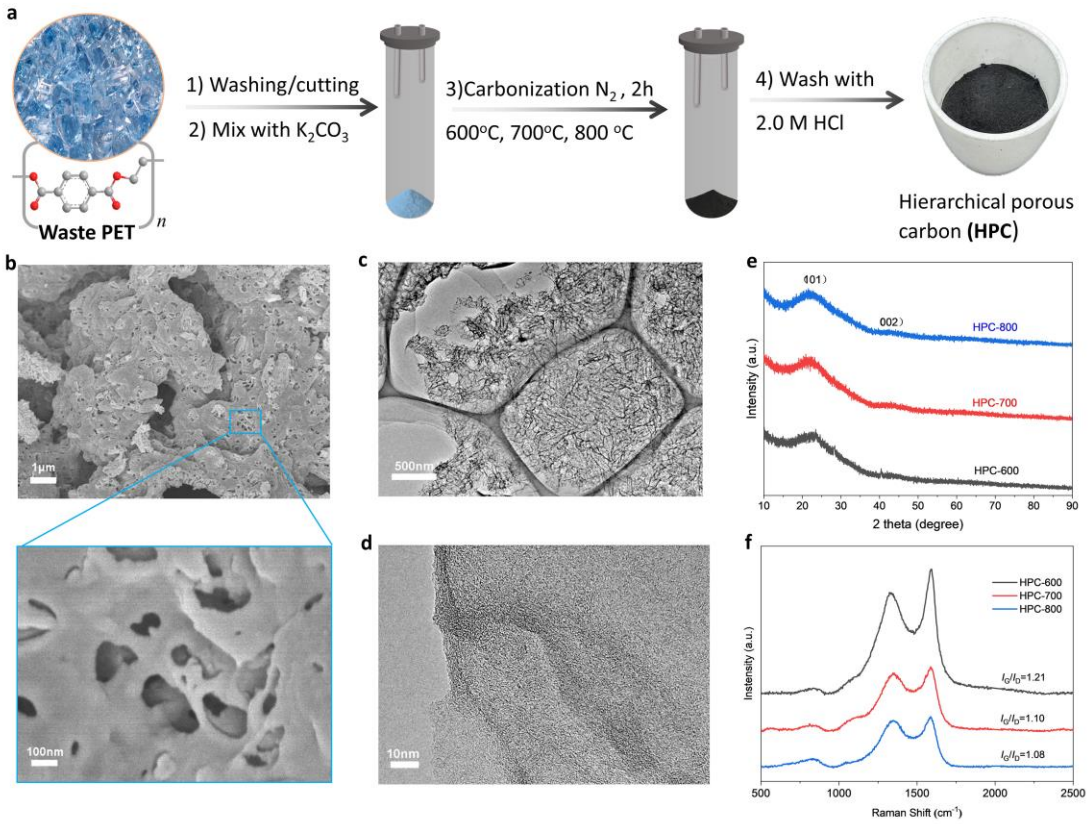

Fig. 2. a) Schematic illustration for the synthetic route to hierarchical porous carbon (HPC) from waste PET. b) SEM images and c, d) TEM images of HPC-700, and e) X-ray diffraction curves and f) Raman

spectroscopy of HPC prepared at varied temperatures.

The microstructure of the obtained materials was first characterized by both SEM and TEM. The SEM images of HPC-700 (**Fig. 2b**) exhibit a rough and porous morphology, with many irregular pores on the surface, and these pores appear interconnected. Such a cross-linked architecture is confirmed by its TEM images, where many small black and white dots further indicate the presence of mecropores (**Figs. 2c**, and **2d)**. These mesopores are generated by the templating effect of potassium carbonate. The three-dimensional (3D) interconnected structure is expected to favorably shorten the ion diffusion path, thereby contributing to enhancing its electrochemical performance as an electrode material. [15] Meanwhile, the effects of carbonization temperatures on the morphological structure of HPCs were fully investigated. HPC-600 (**Figs. S1**a and **S1**b) displays an interconnected sheet-like structure with plenty of macropores, although they are unevenly distributed, less in number and larger in size compared to HPC-700. Besides, the elemental mappings of the HPC-700 material (**Figs. S1**c-e) show that oxygen is uniformly doped into the whole carbon structure, indicative of the formation of an oxygen-containing hierarchical porous carbon.

XRD was further performed to investigate the crystalline structure of the HPC samples. The un-reacted K_2CO_3 are the only remaining species after high-temperature treatment (**Fig. S2**a). Overall, all three HPCs exhibit two distinct diffraction peaks at 21.9° and 43.6°, which correspond to the graphite (002) and (101) planes, respectively (**Fig. 2**e).[16, 17] Compared to the standard graphite peak at 26.6°, the (002) diffraction peak of HPC is noticeably shifted to a lower angle, indicating an increased interlayer spacing according to the Bragg equation ($2d \sin\theta = \lambda$). This enlargement in interlayer spacing is primarily attributed to the intercalation of K atoms from the chemical activation of K_2CO_3 during high-temperature carbonization.[18]

The carbon phase structure of HPCs was further characterized by Raman spectroscopy (**Fig. 2**f). The 1586 cm^{-1} peak (*G* band) corresponds to ordered carbon structures with an sp^2 electronic configuration, while the 1350 cm^{-1} peak (*D* band) is linked to disordered sp^3 hybridized carbon structures resulting from impurities and defects.[19] The intensity ratio of I_G/I_D

can reflect the degree of graphitization in carbon materials – that is, a higher ratio indicates a higher degree of graphitization.[20] The I_G/I_D ratios of the HPC-600, HPC-700, and HPC-800 are 1.21, 1.10 and 1.08, respectively. This means that with increasing temperature, the degree of graphitization gradually decreases and then levels off while the level of defects increases. Generally, a higher degree of graphitization is more beneficial for promoting electron transport and thus enhancing electrochemical performances of the HPC.[21]

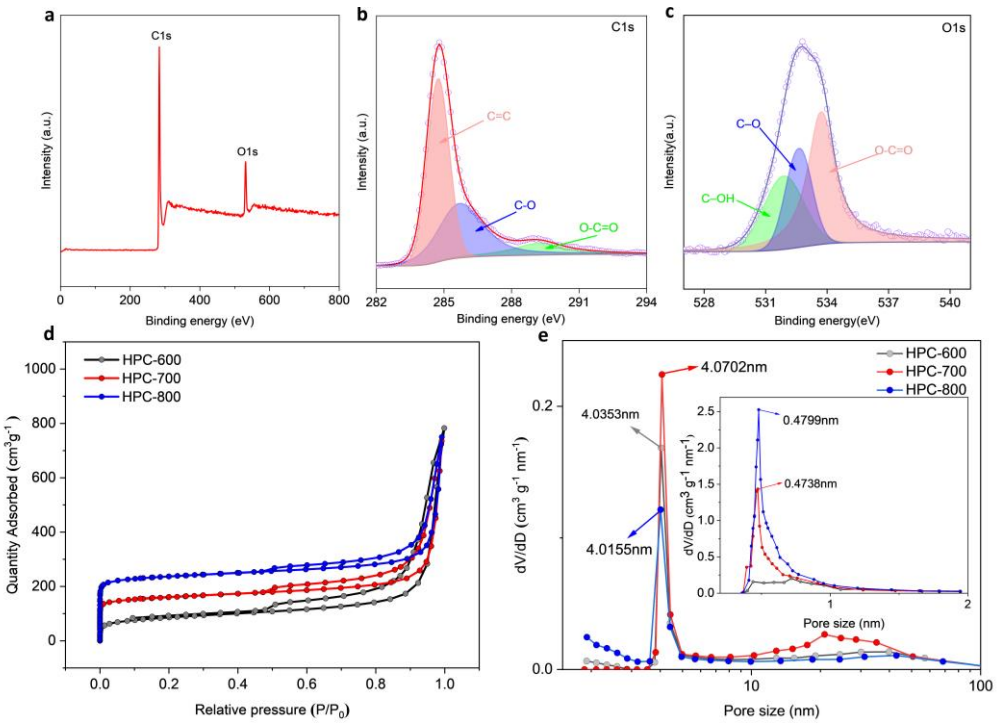

Fig.3. a-c) XPS survey spectrum of HPC-700, d) N_2 adsorption-desorption isotherms and e) pore size distributions of HPC-600, HPC-700 and HPC-800.

Table 1 The specific surface area and porous structure parameter of the samples.

Sample	S_{BET} (m^2 g^{-1})	S_{mic} (m^2 g^{-1})	V_{mic} (cm^3 g^{-1})	V_{mec} (cm^3 g^{-1})	V_t (cm^3 g^{-1})	D_{ave} (nm)
HPC-600	309.05	160.96	0.0711	0.8307	0.9524	13.93
HPC-700	607.72	439.03	0.1737	0.9597	1.1334	7.2546
HPC-800	919.80	781.84	0.3080	0.4838	0.7918	4.8819

Chemical compositions and detailed bonding information of the as-prepared HPCs were analyzed by XPS. Only elemental carbon and oxygen were detected near the surface of the samples, and their relative contents are presented in **Table S2**. The HPC-700 sample comprises 89.3at.% carbon and 10.7at.% oxygen (**Fig. 3**a). The C1s spectra of HPC-700 (**Fig. 3**b) are fitted into three peaks at 284.7, 285.7 and 289.3 eV, corresponding to C = C, C–O and O–C=O, respectively.[22, 23] The O1s spectrum (**Fig. 3**c) reveals three peaks at 531.9 eV (C–OH), 532.6 eV (C-O), and 533.7 eV (O=C-O).[24] The deconvoluted spectra of HPC-600 and HPC-800 are shown in Fig. S3. The presence of oxygen in the samples can be attributed to the incomplete activation of oxygen-containing functional groups in the waste PET. It is worth mentioning that oxygen-containing functional groups can participate in redox reactions, which not only contributes to pseudo-capacitance, but enhance the wettability of carbon materials.[25]

The surface area and pore size distribution of the HPC samples were analyzed through N_2 adsorption and desorption isotherms. The N_2 adsorption-desorption isotherms show similar shapes, characteristic of a typical Type IV curve (**Fig. 3**d).[26] The sharp increase in adsorption volume at low pressure ($P/P_0 < 0.1$) indicates the presence of abundant micropores.[27] The distinct H4 hysteresis loop observed at P/P_0 = 0.45-0.90 indicates the presence of ample mesopores in the sample.[28] The sharp increase in adsorption at high relative pressures ($P/P_0 >$ 0.95) is attributed to the formation of macropores during activation.[29] The pore size distribution curves of the material were calculated using the Barrett-Joyner-Halenda (BJH) and Horvath-Kawazo (HK) models. The pore volumes of the HPC samples are mainly concentrated around 0.47 and 4 nm (**Fig. 3**e). The specific surface area and pore structure parameters of the as-prepared HPC samples are presented in **Table 1**. As temperature increases, the specific surface area of HPC samples increases from 309.05 $m^2 g^{-1}$ (HPC-600) to 602.72 $m^2 g^{-1}$ (HPC-700), finally reaching 919.8 $m^2 g^{-1}$ (HPC-800). To elucidate the reaction process, thermogravimetric analysis (TGA) was performed on the mixture of K_2CO_3 and PET (**Fig. S2**b). At temperatures below 100°C, the initial weight loss is primarily attributed to the evaporation of adsorbed water. Polyethylene terephthalate (PET) begins to decompose at around 390°C. In the presence of

K_2CO_3, the weight loss of the mixture below 600°C is significantly reduced due to the in-situ templating effect of K_2CO_3, which promotes the formation of numerous mesopores. As the temperature increases, a redox reaction involving K_2CO_3 occurs at 600°C, with the reaction:[30]

$$K_2CO_3 + 2C \rightarrow 2K + 3CO$$

$$K2CO_3 \rightarrow K_2O + CO_2$$

The corrosion of the carbon framework by potassium carbonate and the generation of gases results in the formation of numerous micropores. Additionally, K_2O also acts as a template to create many macropores. At temperatures exceeding 774°C, potassium vapor penetrates the carbon structure, expanding the interlayer spacing of carbon atoms and increasing the pore volume of the material. Furthermore, as the temperature rises, the reaction rate accelerates, causing many mesopores to gradually transition into macropores.

3.2. Electrochemical characterization

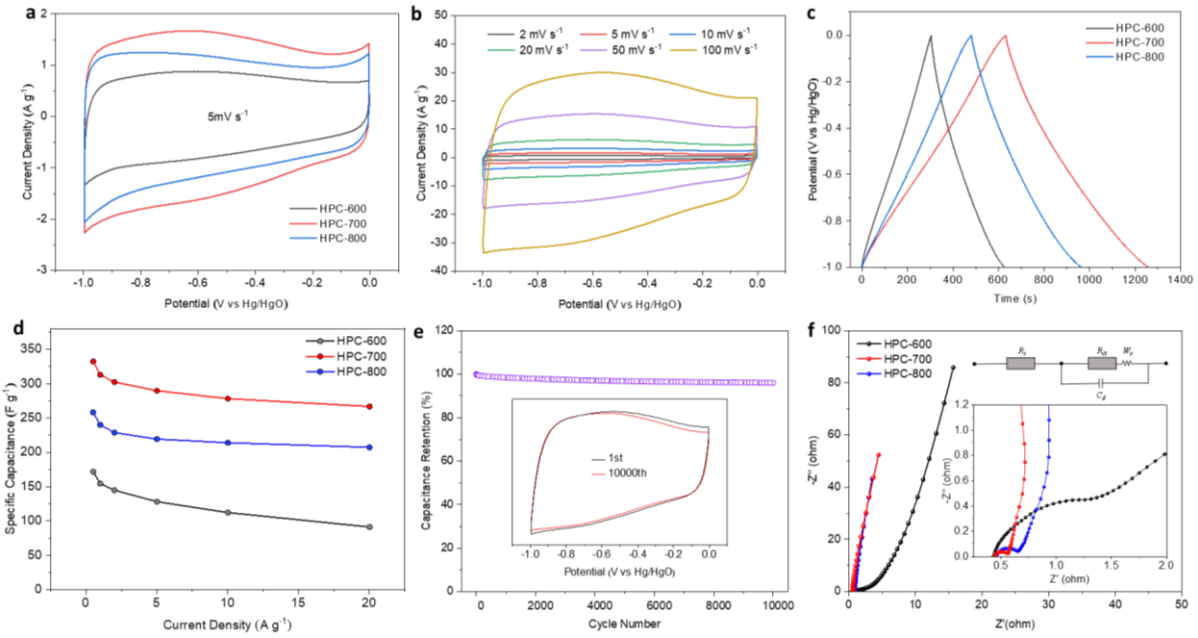

Fig. 4. (a) CV curves of HPC-600, HPC-700 and HPC-800 at 5 mV s^{-1}; (b) CV curves of the HPC-700 electrode at various scan rates; (c) GCD curves of HPC-600, HPC-700 and HPC-800 at 0.5 Ag^{-1}; (d) Specific capacitance of HPC-600, HPC-700 and HPC-800 at different current densities; (e) Cycling performance of HPC-700 at 200mV s^{-1}; (f) Nyquist plots of the HPC-600, HPC-700 and HPC-800 electrodes.

Table 2 Comparison of specific capacitance of HPC-700 with carbon materials reported previously

Carbon precursor	Methods	Carbon Yield (%)	S_{BET} (m^2 g^{-1})	Electrolyte	Specific capacitance (F g^{-1} @ A g^{-1})	Capacitance retention	Ref.
Fulvic acid	450°C Carbonization and KOH activation	14.5	1938	1 M Et_4NBF_4/PC	107@2.5	97% after 20000 cycles	31
Starch	700°C Carbonization and KOH activation	32	3182	6M KOH	316@1	92.5% after 10000 cycles	32
Wood tar	crab shell template and KOH activation	18.22	1898	6M KOH	338.5@1	95% after 5000 cycles	33
Sawdust	H_3PO_4 activation	30.24	1281.6	1 M H2SO4	169.4@0.5	98.3% after 5000 cycles	34
Walnut shells	500°C Carbonization and KOH activation	23	3577	6M KOH	330@0.1	95% after 10000 cycles	35
Lentinula edodes	400°C Carbonization and KOH activation	36.09	1569.3	6M KOH	375@0.5	94.1% after 10000 cycles	36
Ramie	KOH activation	31.33	3034.56	1 M Et_4NBF_4/AN	39.03@40	92.01% after 10000 cycles	37
Algae and bamboo	Na_2CO_3-K_2CO_3 activation	22.2	1326.58	6M KOH	306.2@0.25	91% after 5000 cycles	38
Commercial YP-50F	NA	NA	1410	6M KOH	170@0.5	78% after 5000 cycles	39
Commercial YP-80F	NA	NA	2361	6M KOH	168@1	NA	40
PP	Melamine dopant and $ZnCl_2$ activation	34.3	1037.1	6M KOH	224.8@1	91.2% after 50000 cycles	41
PE	600°C Carbonization and KOH activation	45	3059	6M KOH	355@0.2	82.4% after 5000 cycles	1
PET	KOH activation	18	1737.5	1 M Et_4NBF_4/AN	25.9@0.5	90.1% after 2500 cycles	42
PET	MgO template and KOH activation	17	1863.55	2M KOH	191.4@0.2	98.2% after 5000 cycles	11
PET	MgO/$Co(acac)_3$ template	36.4	561	6M KOH	210.5@0.5	90.1% after 5000 cycles	12
PET	K_2CO_3 template	33.45	607.72	6M KOH	332.3@0.5	95.95% after 10000 cycles	This work

The electrochemical performances of different HPC samples were tested in a three-electrode system. The cyclic voltammetry (CV) measurements conducted at a scan rate of 5 mV s^{-1}

revealed that all HPC samples exhibited rectangular-shaped curves (**Fig. 4**a), indicating their ideal electrochemical performance. Calculations based on the CV curves of HPC-700 indicate that it exhibits the highest integrated area, suggesting its superior specific capacitance. The weak peak observed in the voltage window of 1V to 0.4V is attributed to the REDOX reactions of oxygen-containing functional groups, although its contribution is negligible compared to the double-layer capacitance.[43] At a scan rate of 100 mV s^{-1}, the CV curve of HPC-700 maintains a rectangular shape, indicating rapid ion and charge transfer rates across the entire electrode (**Fig. 4**b). **Fig. 4**c shows the GCD curves of the sample at 0.5 A g^{-1}, the constant current charge-discharge curves of all samples exhibit typical triangular shapes, indicating that double-layer charge storage predominates.

According to Eq. (1), HPC-700 exhibits a specific capacitance of 332.27 F g^{-1} at 0.5 A g^{-1}, which is higher than 258.13 F g^{-1} of HPC-800 and 171.73 F $g^{-}1$ of HPC-600. Generally, the specific surface area (SSA) plays a crucial role in enhancing capacitance, as the carbon electrode with higher SSA values have more sites for ion accumulation through electrostatic interactions. The specific surface area is typically significantly contributed by micropores. The low capacitance of HPC-600 is caused by its low SSA value, which provides insufficient active sites. As shown in **Fig. 3e**, the micropore peaks of HPC-700 and HPC-800 are both approximately 0.47 nm close to the size of hydrated K^+ ions (0.331 nm). When the ion size matches the pore size, the corresponding porous carbon materials in EDLCs can achieve the maximum specific capacitance due to the strong effect arising from intense interactions between ions and the pore walls[39]. However, for HPC-800, 80.9% of its specific surface area is contributed by micropores, and the lack of sufficient mesopores for providing ion channels make it difficult for some electrolyte ions to enter these pores and form double layers, resulting in a large portion of the ineffective specific surface area. Therefore, an appropriately designed hierarchical porous structure plays a key role in improving the specific capacitance of electrode materials. Furthermore, HPC-700 exhibits a specific capacitance of 266.67 F g^{-1} with a retention rate of 80.3% at 20 A g^{-1}, significantly surpassing HPC-600 (53.2%) and HPC-800 (80.2%), demonstrating excellent rate performance (**Fig. 4**d). The CV testing was conducted

on the HPC-700 electrode with a scan rate of 200 mV s^{-1} (**Fig. 4**e). The results indicate a capacitance retention rate of 95.98% after 10,000 cycles. The CV curve maintained its original shape without significant changes, demonstrating its excellent cycling stability.

To better understand the cause of capacitance degradation, we examined the microstructure of the electrode material before and after cycling. After 10,000 cycles, the microstructure was destroyed, the pore size increases, and the pores deepened (**Fig. S**4). This led to a longer or more uneven ion diffusion path within the electrode material, which affected the electrochemical performance of the electrode. The Nyquist plots of HPCs (**Fig. 4**f) consist of a semicircle in the high-frequency region and a vertical line in the low-frequency region. The intersection point value with the real axis represents the combined series resistance (R_s), and all HPC samples exhibit low R_s. According to the results of the equivalent circuit model, the semicircle of the HPC-700 electrode is the smallest, and the diameter of the semicircle represents the charge transfer resistance (R_{ct}). This indicates that its R_{ct} (0.0658 Ω) is lower than that of the HPC-600 (0.495 Ω) and HPC-800 (0.115 Ω). The low-frequency region of the curve is governed by mass transfer control, with HPC-700 exhibiting a steeper slope than other samples, indicating faster ion diffusion. Hence, HPC-700 has the best electrical conductivity and ion permeability among the HPC samples. **Table 2** presents the electrochemical performance data of other materials. Compared to other biomass-based porous carbons and commercial porous carbons, HPC-700 exhibits excellent capacitance, attributed to its unique hierarchical porous structure. In addition, it demonstrates outstanding cycling stability. Other preparation methods often require pretreatment and the use of highly corrosive chemicals as activators, leading to a single pore structure, significant resource waste, and a reduced yield. In contrast, HPC-700 gives rise to a high yield of 32.2% (**Fig. S2**c). The one-pot method utilizing potassium carbonate is not only simple and energy-efficient but also facilitates the formation of a unique hierarchical porous structure in the porous carbon.

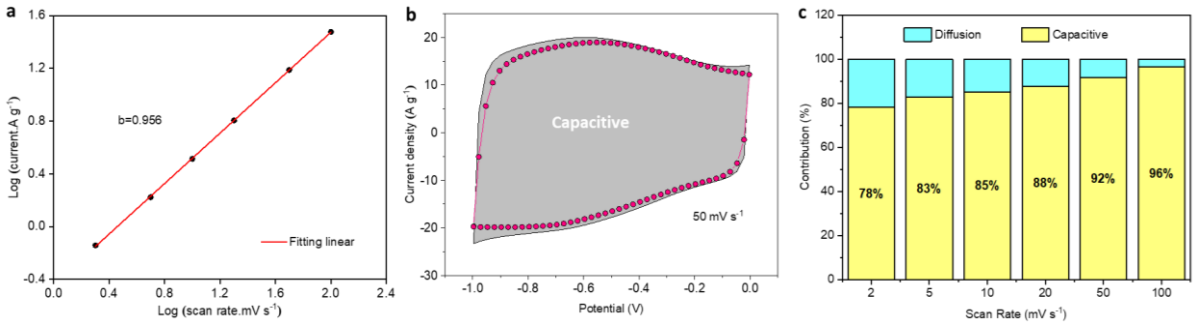

Fig. 5. (a) The b-value obtained from the CV curves of HPC-700 at various scan rates; (b) The contributions of EDLC and PC of HPC-700 at 50 mV s^{-1}; (c) The capacitive and diffusion contribution ratios at various scan rates.

Based on the charge storage mechanism, the specific capacitance of supercapacitors is categorized into C_s and C_d, representing surface-controlled and diffusion-controlled capacitances, respectively. C_s includes electric double-layer capacitance (EDLC) from electrolyte absorption/desorption and Faradaic pseudo-capacitance from redox reactions.[44] Eq.(4) illustrates the storage mechanism of supercapacitors, showing that at a constant voltage, the current i varies exponentially with the scan rate ν, where i represents the current and ν denotes the scan rate. The parameter b ranges from 0.5 to 1. When b=0.5, charge storage is predominantly dominated by diffusion control, whereas b=1 indicates a surface-controlled process. In **Fig.5a**, the calculated b value for HPC-700 is 0.956 ± 0.004, indicating a predominant surface-controlled charge/discharge behavior because of its distinctive hierarchical porous structure. Furthermore, to quantitatively elucidate the electrochemical kinetics of supercapacitors based on HPC-700, the capacitive and diffusion types are further calculated according to equations (6) or (7) [45] :

$$i = a\, v^b \tag{5}$$

$$i = k_1 v + k_2 v^{0.5} \tag{6}$$

$$i v^{-0.5} = k_1 v^{0.5} + k_2 \tag{7}$$

Here, $k_1 v$ and $k_2 v^{0.5}$ represent capacitive-controlled and diffusion-controlled currents, respectively. $k_1$and $k_2$are the slope and intercept of the $iv^{-0.5}$and $v^{0.5}$curve, respectively. Therefore, the contributions of capacitance and diffusion control to the total capacity can be estimated at various scan rates. **Fig. 5b** and **S5** illustrate the contributions of EDLC (electric

double-layer capacitance) and PC (pseudo-capacitance). The capacitance contribution rates of HPC-700 are displayed (**Fig. 5**c) across scan rates ranging from 2 to 100 mV s^{-1}: at 2 mV s^{-1} (low scan rate), the capacitance contribution rate is 78.2%, increasing to 96.4% at 100 mV s^{-1} (high scan rate). As the scan rate increases, the influence of diffusion-controlled processes on charge storage gradually diminishes. Additionally, surface-controlled behavior not only indicates charge storage capacity but signifies the performance of supercapacitors. A higher contribution rate of surface-controlled capacitance indicates a better rate capability.

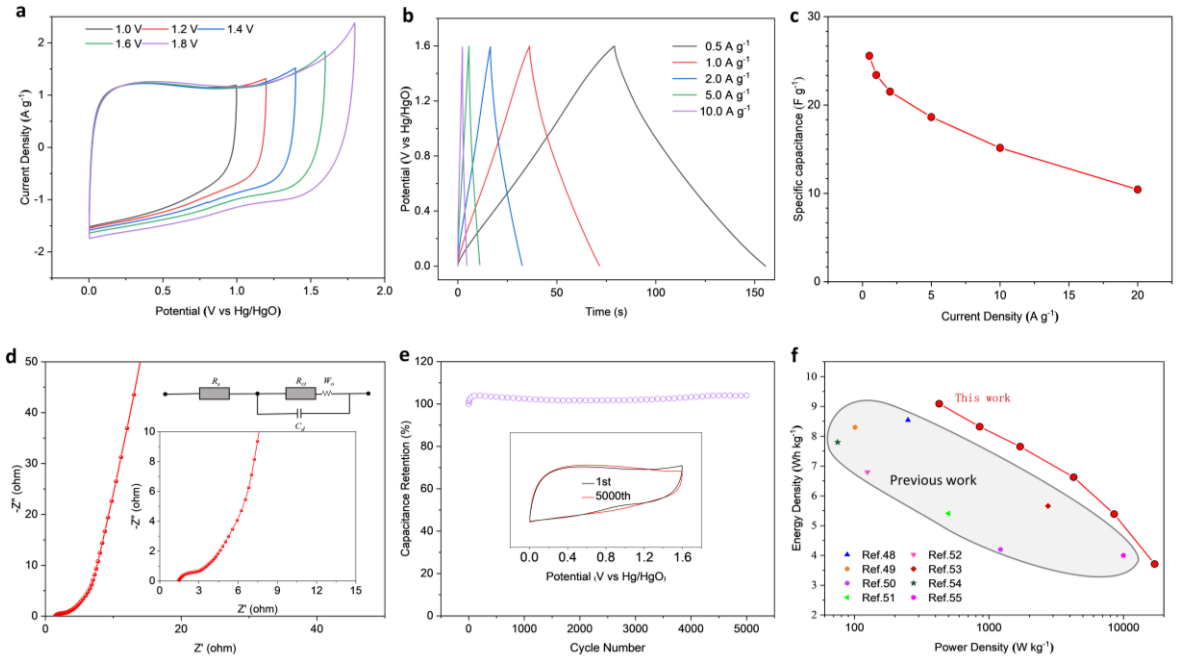

Fig. 6. Electrochemical performances of HPC-700// HPC-700 symmetric two-electrode supercapacitors: (a) CV curves at 50 mV s^{-1} in various voltage windows; (b) GCD curves at different current densities; (c) Specific capacitance at different current densities; (d) Nyquist plot; (e)Cycling performance in 1.6 V at 200 mV s^{-1}; (f) Ragone plot.

To further evaluate the double-layer performance of HPC-700, a symmetrical dual-electrode capacitor was assembled using a 1M Na_2SO_4 solution as the electrolyte. Compared to acidic or alkaline electrolytes, neutral electrolytes offer manufactured supercapacitors higher operating voltages, which are advantageous for achieving greater energy densities.[46] **Fig. 6**a depicts the CV curves of HPC-700//HPC-700 supercapacitors at different operating voltages ranging from 1.0 to 1.8 V. Significantly, the anomalous increase in anodic current from 0 to 1.8

V suggests electrolyte decomposition, while this phenomenon is absent from 0 to 1.6 V. **Fig. 6**b illustrates the GCD curves at current densities ranging from 0.5 A g^{-1} to 10 A g^{-1}. These triangular curves maintain a linear and symmetrical shape without notable deformation, indicating an ideal capacitance performance of the HPC-700//HPC-700 system. **Fig. 6**c shows the relationship between current density and specific capacitance calculated from the GCD curves. The symmetric electrode device exhibits a capacitance of 25.57 F g^{-1} at 0.5 A g^{-1} and maintains 10.44 F g^{-1} at 20 A g^{-1}, resulting in a capacitance retention rate of 40.83%.

The Nyquist plot of the device is shown in **Fig. 6**d, the R_s and R_{ct} values of HPC-700 are 1.50 Ω and 0.80 Ω, which represents the excellent capacity of charge transfer and capacitance behavior. The cycling performance of the HPC-700//HPC-700 symmetric supercapacitor is shown in **Fig. 6**e. After 5000 cycles at 200 mV s^{-1}, the capacitance retention rate of the HPC-700//HPC-700 symmetric supercapacitor reached 104%, demonstrating outstanding electrochemical stability. The slight increase in capacitance observed during cycling measurements is probably attributed to effective electrolyte diffusion through open channels in the electrode material, indicating an excellent cycling stability performance of the HPC-700 electrode. **Fig. 6**f depicts the relationship between power density and energy density of the HPC-700 symmetric supercapacitor. The energy density was calculated to be 9.09 W h kg^{-1} at 426.7 W kg^{-1} power density. When employed in supercapacitors, it demonstrates a comparatively higher energy density compared to previously reported porous carbons and graphene nanomaterials.[47-54]

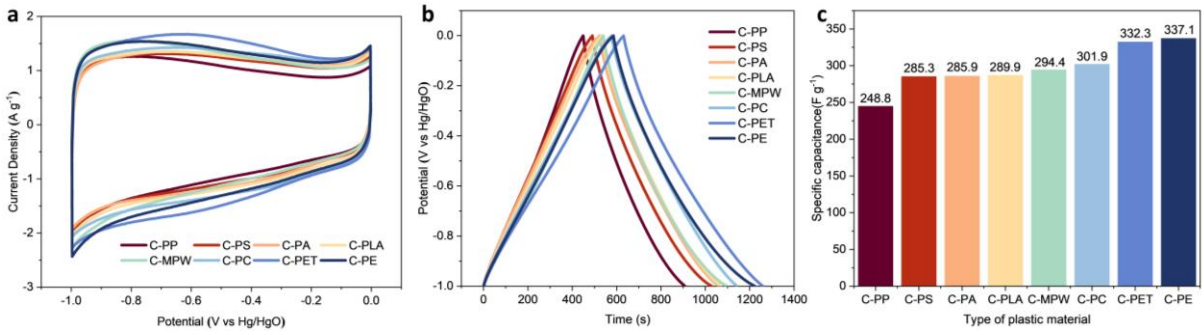

Fig.7. The porous carbons prepared from different plastics were tested in a three-electrode system. (a) CV response of carbon materials depicting quasi-rectangular shape. Recorded at the scan rate of 5 mV s^{-1}. (b)

GCD response of carbon materials at the current density of 0.5 A g^{-1}. (c) Difference of specific capacitance on carbon materials made from various polymer materials.

To further demonstrate the applicability of this method to other waste plastics, we tested the electrochemical performance of porous carbons derived from different waste plastics, with the tests conducted in 6M KOH. The CV curves in **Fig. 7a** all exhibit a standard rectangular shape, indicating a nearly ideal EDLC behavior. The weak peak observed within the 0.5V voltage window corresponds to the Faradaic pseudocapacitance attributed to oxygen-containing groups in the carbon structure. In **Fig. 7**b, all GCD curves show a typical triangular shape, indicating that double-layer charge storage dominates. Based on the discharge time, C-PE demonstrates the longest discharge time, suggesting the highest capacitance. **Fig. 7c** presents the capacitance of porous carbons derived from all tested waste plastics, with values generally exceeding 250 F g^{-1}, confirming the applicability of this method to other waste plastics.

3.3 Life cycle impact assessment and interpretation

Fig. 8 shows the relative ecological impact of each step in the HPC-700 preparation process, with the full impact results for the 10 impact categories summarized in Table S3. Carbonation has the greatest environmental impact during preparation, especially for GWP and ADP, due to direct CO_2 emissions and K_2CO_3 utilization in the process. Nevertheless, HPC-700 has a GWP of about 13.5kg CO_2/kg, which is comparable to porous carbon prepared from other organic solids and plastic wastes (11.1–13.3 kg CO_2/kg) [55] and it has a significantly lower impact on global warming compared to other recycling methods. The CED of the process is about 148.1 MJ/kg, which is also lower than some biomass activation for the preparation of porous carbon[56, 57]. This explains the lower energy consumption of the experiment, which has a comparative advantage with other two-step pyrolysis methods. The LCA results clearly show the feasibility of the preparation of porous carbon in this study.

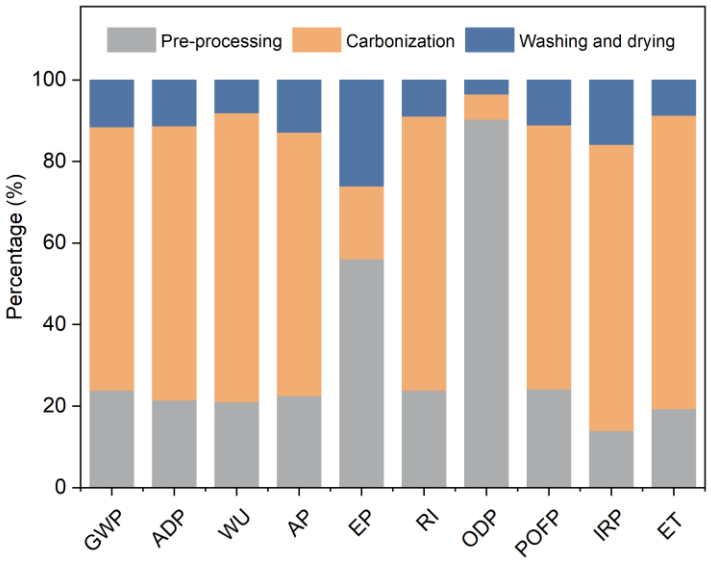

Fig. 8. The relative ecological impact of each step during HPC-700 preparation process.

Unfortunately, a significant limitation of the LCA method is the absence of comprehensive databases for certain chemicals and processes in OpenLCA. Despite this, the method remains effective in assessing the environmental impact of the preparation process of porous carbon. Variations in LCA results can often be attributed to discrepancies in materials or processes across different databases. In addition, the data used in LCA studies primarily come from previous literature, laboratory-scale experimental data, and publicly available data from companies. However, the complexity of laboratory data cannot be compared to that of actual industrial production. In future research, more precise measurements of the components should be conducted.

4. Conclusions

In summary, this work has developed a facile effective carbonization method that can convert waste PET into hierarchical porous carbon for supercapacitor applications. The resulting HPC material exhibits a distinctive hierarchical porous structure with a desired specific surface area and abundant oxygen content. This unique structure enables the electrode to achieve a high specific capacitance of up to 332 F g^{-1} at a current density of 0.5 A g^{-1}. The assembled HPC-700//HPC-700 symmetric supercapacitor exhibits an energy density of up to

9.09 Wh kg^{-1} and demonstrates an excellent cycling stability in a 1 M Na_2SO_4 aqueous electrolyte. This work presents another promising approach to recycling waste PET plastics to high-performance porous carbon materials, which hold great potential for applications as energy storage materials, such as advanced supercapacitors.

Acknowledgements

The present work was supported by the Fundamental Research Funds for the Central Universities (No. 2572023CT10), and the Australia - UK Renewable Hydrogen Innovation Partnerships (No. AUKRH000031).

References

1. H. Zhang, X. L. Zhou, L. M. Shao, F. Lü and P. J. He, *ACS Sustain. Chem. Eng.*, 2019, **7**, 3801-3810.
2. J. R. Anusha, T. Citarasu, G. Uma, S. Vimal, C. Kamaraj, V. Kumar, K. Muzammil and M. Mani Sankar, *Chemosphere*, 2024, **352**, 141417.
3. X. Bian, G. Xia, J. H. Xin, S. Jiang and K. Ma, *Chemosphere*, 2024, **350**, 141076.
4. V. Tournier, C. M. Topham, A. Gilles, B. David, C. Folgoas, E. Moya-Leclair, E. Kamionka, M. L. Desrousseaux, H. Texier, S. Gavalda, M. Cot, E. Guemard, M. Dalibey, J. Nomme, G. Cioci, S. Barbe, M. Chateau, I. Andre, S. Duquesne and A. Marty, *Nature*, 2020, **580**, 216-+.
5. J. J. Cao, H. X. Liang, J. Yang, Z. Y. Zhu, J. Deng, X. D. Li, M. Elimelech and X. L. Lu, *Nat. Commun.*, 2024, **15**, 12.
6. N. N. Loganathan, V. Perumal, B. R. Pandian, R. Atchudan, T. Edison and M. Ovinis, *J. Energy Storage*, 2022, **49**, 22.
7. Y. F. Yin, Q. J. Liu, Y. T. Zhao, T. T. Chen, J. Wang, L. Gui and C. Y. Lu, *Energy Fuels*, 2023, DOI: 10.1021/acs.energyfuels.2c04093, 32.
8. Y. F. Shen and Y. P. Zhu, *J. Mater. Chem. A*, 2024, **12**, 6211-6242.
9. G. Nath, P. K. Singh, P. S. Dhapola, S. Dohare, I. M. Noor, T. Sharma and A. Singh, *Biomass Convers. Biorefinery*, 2024, **14**, 7635-7642.
10. K. K. R. Reddygunta, A. Callander, L. Siller, K. Faulds, L. Berlouis and A. Ivaturi, *RSC Adv.*, 2024, **14**, 12781-12795.
11. S. Q. Chen, S. Y. Fang, A. I. Lim, J. M. Bao and Y. H. Hu, *Chemosphere*, 2023, **322**, 9.
12. X. Y. Mu, Y. H. Li, X. G. Liu, C. D. Ma, H. Q. Jiang, J. Y. Zhu, X. C. Chen, T. Tang and E. Mijowska, *Nanomaterials*, 2020, **10**, 13.
13. X. Zhou, L. Zhu, W. Dong and M. Jiang, *Chemosphere*, 2023, **345**, 140546.
14. B. Ray, S. R. Churipard, A. Cherevotan, D. R. Deka, D. Goud, H. Kopperi and S. C. Peter, *J. Mater. Chem. A*, 2024, **12**, 30309-30317.
15. H. H. Bi, X. J. He, H. F. Zhang, H. Q. Li, N. Xiao and J. S. Qiu, *Renew. Energy*, 2021, **170**, 188-196.
16. L. Lu, V. Sahajwalla, C. Kong and D. Harris, *Carbon*, 2001, **39**, 1821-1833.
17. A. Sharma, T. Kyotani and A. Tomita, *Carbon*, 2000, **38**, 1977-1984.
18. Y. Lu, J. N. Liang, S. F. Deng, Q. M. He, S. Y. Deng, Y. Z. Hu and D. L. Wang, *Nano Energy*, 2019, **65**, 9.

19. M. Y. Zhang, Y. Sun and R. J. Song, *Microporous Mesoporous Mat.*, 2022, **330**, 9.
20. R. J. Hu, R. Y. Li, S. N. Tan and R. J. Song, *ChemistrySelect*, 2023, **8**, 10.
21. B. J. Gang, F. Zhang, X. L. Li, B. Zhai, X. Y. Wang and Y. Song, *J. Energy Storage*, 2021, **33**, 9.
22. L. Yao, J. S. Lin, H. T. Yang, Q. Wu, D. R. Wang, X. J. Li, L. B. Deng and Z. J. Zheng, *Nanoscale*, 2019, **11**, 11086-11092.
23. F. Mo and X. L. Wu, *J. Energy Storage*, 2022, **54**, 7.
24. N. Rey-Raap, M. A. C. Granja, M. F. R. Pereira and J. L. Figueiredo, *Electrochim. Acta*, 2020, **354**, 13.
25. L. Hao, X. L. Li and L. J. Zhi, *Adv. Mater.*, 2013, **25**, 3899-3904.
26. S. Dong, X. J. He, H. F. Zhang, X. Y. Xie, M. X. Yu, C. Yu, N. Xiao and J. S. Qiu, *J. Mater. Chem. A*, 2018, **6**, 15954-15960.
27. A. L. Shen, Y. Q. Zou, Q. Wang, R. A. W. Dryfe, X. B. Huang, S. Dou, L. M. Dai and S. Y. Wang, *Angew. Chem.-Int. Edit.*, 2014, **53**, 10804-10808.
28. M. Y. Yuan, L. H. Liu, B. Niu, F. Jiang and M. Li, *Int. J. Electrochem. Sci.*, 2019, **14**, 4034-4046.
29. X. G. Liu, Y. L. Wen, X. C. Chen, T. Tang and E. Mijowska, *Sci. Total Environ.*, 2020, **723**, 11.
30. H. Wang, Y. Yuan, F. Q. Xiong, B. L. Ma, J. M. Yang, Y. Qing, F. X. Chu and Y. Q. Wu, *Chem. Eng. J.*, 2023, **476**, 13.
31. J. R. Wang, C. Zhang, Z. J. Chen, J. S. Dong, P. P. Chang, T. Yang, J. Z. Zhang and P. Y. Zhao, *Diam. Relat. Mat.*, 2024, **149**, 10.
32. X. L. Zhou, L. Y. Zhu, Z. Li, Y. Yang, X. J. Qian, A. M. Xu, M. Jiang and W. L. Dong, *Biomass Convers. Biorefinery*, 2023, DOI: 10.1007/s13399-023-03942-2, 12.
33. J. Wu, M. W. Xia, X. Zhang, Y. Q. Chen, F. Sun, X. H. Wang, H. P. Yang and H. P. Chen, *J. Power Sources*, 2020, **455**, 9.
34. G. F. Lin, Q. Wang, X. Yang, Z. H. Cai, Y. Z. Xiong and B. Huang, *RSC Adv.*, 2020, **10**, 17768-17776.
35. T. X. Shang, Y. Xu, P. Li, J. W. Han, Z. T. Wu, Y. Tao and Q. H. Yang, *Nano Energy*, 2020, **70**, 7.
36. B. Geng, Y. J. Zou, F. Xu, L. X. Sun and C. L. Xiang, *J. Energy Storage*, 2024, **103**, 10.
37. Q. Wang, Y. X. Qu, J. Bai, Z. Y. Chen, Q. T. Luo, H. J. Li, J. Li and W. Q. Yang, *Nano Energy*, 2024, **120**, 11.
38. J. Li, D. Zhong, K. Zeng, X. Chen, B. Y. Wu, T. J. Liu, H. P. Yang and H. P. Chen, *Energy*, 2024, **305**, 9.
39. D. W. Yang, H. J. Jing, Z. W. Wang, J. H. Li, M. X. Hu, R. T. Lv, R. Zhang and D. L. Chen, *J. Colloid Interface Sci.*, 2018, **528**, 208-224.
40. M. Bora, D. Bhattacharjya, S. Hazarika, X. Fan and B. K. Saikia, *Energy Fuels*, 2022, **36**, 14476-14489.
41. L. Q. Qiu, Y. N. Li, M. H. Jiang, H. Zhang, C. Y. Zeng and S. L. Chen, *J. Energy Storage*, 2025, **106**, 9.
42. M. Y. Jung, I. C. Yang, D. Choi, J. W. Lee and J. C. Jung, *Korean J. Chem. Eng.*, 2023, **40**, 2442-2454.
43. B. Yan, L. Feng, J. J. Zheng, Q. Zhang, Y. Z. Dong, Y. C. Ding, W. S. Yang, J. Q. Han, S. H. Jiang and S. J. He, *Appl. Surf. Sci.*, 2023, **608**, 13.
44. Y. G. Wang, Y. F. Song and Y. Y. Xia, *Chem. Soc. Rev.*, 2016, **45**, 5925-5950.
45. D. Dong, Y. S. Zhang, Y. Xiao, T. Wang, J. W. Wang and W. Gao, *Fuel*, 2022, **309**, 10.
46. C. L. Long, X. Chen, L. L. Jiang, L. J. Zhi and Z. J. Fan, *Nano Energy*, 2015, **12**, 141-151.
47. M. G. Ding, R. Haneef, S. H. Wei and W. Gao, *ChemElectroChem*, 2024, **11**, 11.
48. H. Y. Jia, J. F. Zhu, M. Zhang, S. J. Sang, F. Hu and F. Zhang, *J. Energy Storage*, 2021, **38**, 7.
49. X. Li, Y. L. Li, X. D. Tian, Y. Song and Y. M. Cui, *J. Alloy. Compd.*, 2022, **903**, 8.
50. S. C. Abbas, C. M. Lin, Z. F. Hua, Q. D. Deng, H. Huang, Y. H. Ni, S. L. Cao and X. J. Ma, *Chem. Eng. J.*, 2022, **433**, 9.
51. S. P. Lv, X. Y. Wu, Y. Lv, Z. F. Wang, N. Liang, Y. C. Pei, A. Xuhrat and J. X. Guo, *Energy Fuels*, 2023,

37, 12427-12435.
52. T. T. Wang, X. He, W. B. Gong, Z. H. Kou, Y. Yao, S. Fulbright, K. F. Reardon and M. H. Fan, *Fuel Process. Technol.*, 2022, **225**, 11.
53. Y. S. Xu, M. J. Xiao, T. T. Liu, R. P. Lin, Y. S. Meng, Y. Zhang and F. L. Zhu, *J. Electroanal. Chem.*, 2023, **948**, 13.
54. J. Zhou, Z. S. Zhang, W. Xing, J. Yu, G. X. Han, W. J. Si and S. P. Zhuo, *Electrochim. Acta*, 2015, **153**, 68-75.
55. S. J. Li, M. K. Cho, S. Deng, J. Y. Wang and K. B. Lee, *Chem. Eng. J.*, 2024, **494**, 11.
56. C. Li, K. Sun, Y. F. Sun, Y. W. Shao, G. M. Gao, L. J. Zhang, S. Zhang and X. Hu, *Chem. Eng. J.*, 2024, **480**, 14.
57. A. Heidari, E. Khaki, H. Younesi and H. Y. R. Lu, *J. Clean Prod.*, 2019, **241**, 13.

Supporting Information

Converting waste poly(ethylene terephthalate) to hierarchical porous carbon towards high-performance supercapacitor

Kaile Wang,[a] Ruiyang Li, [a] Xuesen Zeng,[b] Pingan Song[c,]*, Jisheng Sun,[d] Rongjun Song [a],*

[a] *Heilongjiang Key Laboratory of Molecular Design and Preparation of Flame Retarded Materials, College of Chemical Engineering and Resource Utilization, Northeast Forestry University, Harbin 150040, PR China*

b Centre for Future Materials, University of Southern Queensland, Toowoomba 4305, Queensland, Australia

c Centre for Future Materials, School of Agriculture and Environmental Science, University of Southern Queensland, Springfield 4300, Queensland, Australia

d Australia Sunlight Group Pty Ltd, Carole Park 4300, Queensland, Australia

* Corresponding author:

E-mail: pingan.song@usq.edu.au, pingansong@gmail.com

E-mail: rongjunsong@nefu.edu.cn

Contents:

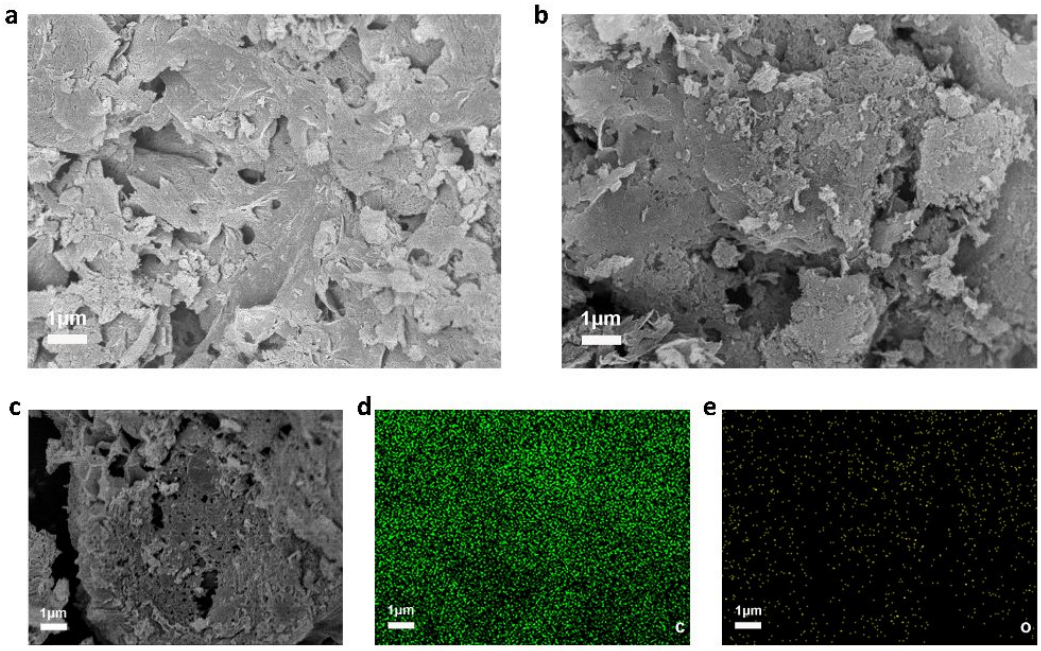

Fig. S1. (a) SEM image of HPC-600. (b) SEM image of HPC-800. (c-e) EDS mapping of HPC-700.

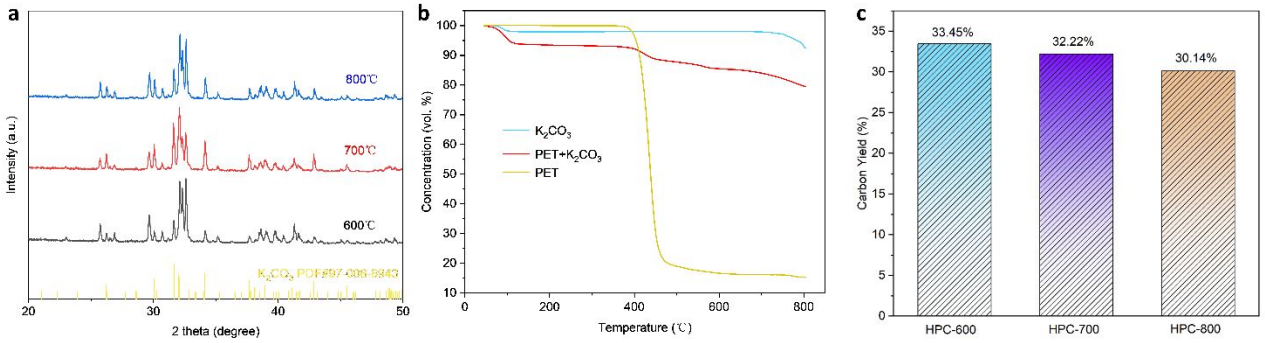

Fig. S2. (a)XRD patterns corresponding to the samples produced from the mixture of PET and K_2CO_3 before washing. (b) TGA curves of K_2CO_3, PET and their mixture. (c) Carbon yield of HPCs.

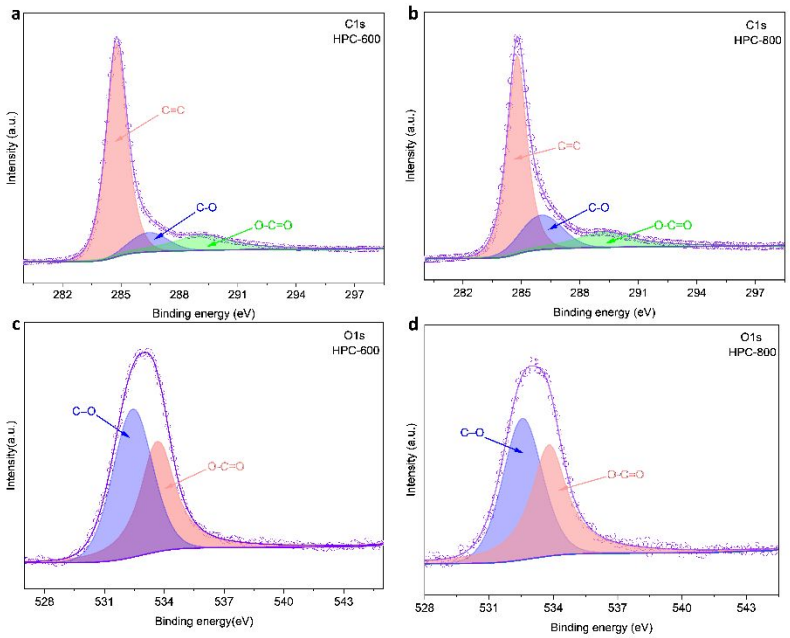

Fig. S3. XPS results of HPC-600 and HPC-800 : (a-b) C1s spectra, (c-d) O1s spectra.

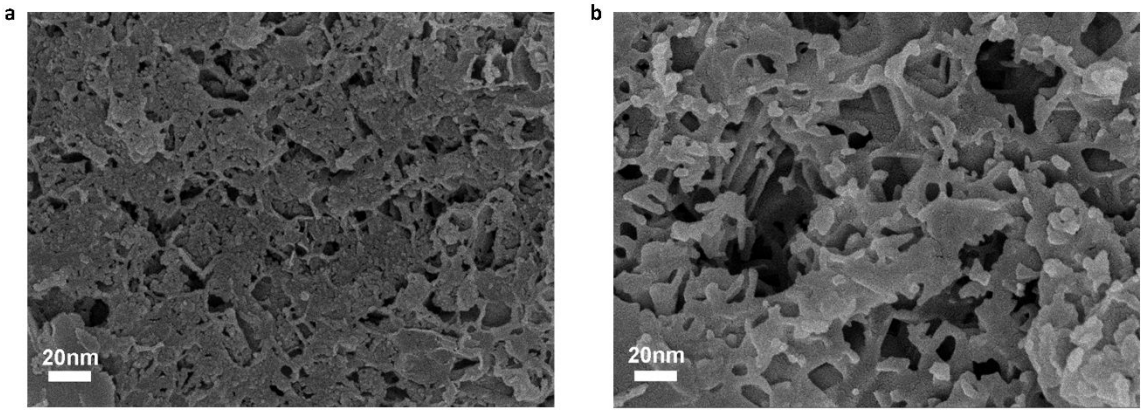

Fig. S4. SEM images of the HPC-700 electrode before (a) and after 10,000 cycles (b).

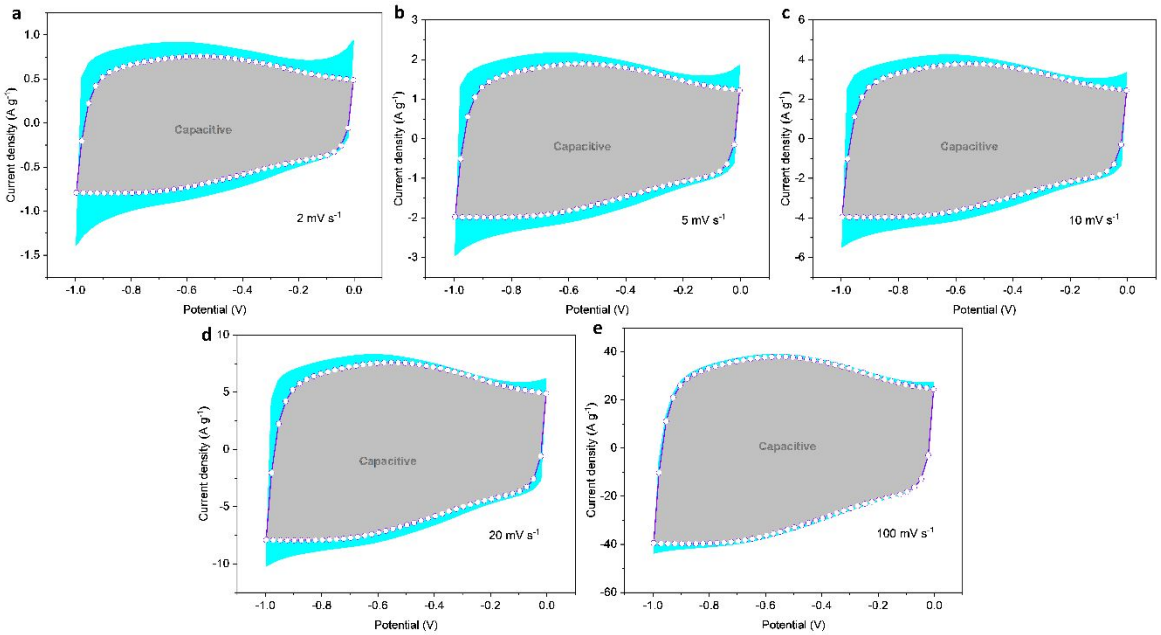

Fig. S5. The contributions of EDLC and PC of HPC-700 at various scan rates.

Table S1 Energy consumption at different stages of the porous carbon preparation process.

Preparation Stage	Temperature/Time	Power (kW)	Energy Consumption (kWh)	Sample Yield (g)	Specific Energy Consumption (kWh/g)
Carbonization Stage	800℃/2 h	1.6	3.2	0.805	3.975
Washing Stage	Room temperature /0.5 h	0.37	0.185	0.805	0.230
Drying Stage	80°C / 3 h	0.6	1.8	0.805	2.236

Table S2 Element composition and content of O functional groups tested from XPS.

Samples	Element composition (at.%)		Content of O functional groups (at.%)		
	C	O	OH	COOH	CO
HPC-600	90.53	9.47	//	4.54	4.93
HPC-700	89.3	10.7	2.92	5.20	2.58
HPC-800	92.63	7.37	//	3.56	3.81

Table S3. Life cycle environmental impact of HPC-700.

Impact category	Preprocessing	Carbonization	Washing and drying	Sum
CED (MJ)	33.6	99.39	15.429	148.419
GWP (kg CO_2 eq)	3.225	8.726	1.549	13.5
ADP (MJ)	34.777	109.0296	18.212	162.0186
WU (kg)	0.703	2.37	0.269	3.342
AP (kg SO_2 eq)	0.0158	0.0453	0.009	0.0701
EP (kg PO43-eq)	0.0082	0.0026	0.0038	0.0146
RI (kg $PM_{2.5}$ eq)	0.0054	0.015233	0.002	0.022633
ODP (kg CFC-11 eq)	9.4578E-08	6.4549E-09	3.6310E-09	1.05E-07
POFP (kg NMVOC eq)	0.011	0.0295	0.005	0.0455
IRP (kg U235 eq)	0.18	0.9045	0.204	1.2885
ET (CTUe)	0.731	2.7196	0.327	3.7776

Data availability statements

All the data supporting this article have already been included in this article and no new data were generated or analysed as part of this article.